High-Efficiency Current Control Methods Based on Multidimensional Feedback Quantization and Its Application to Three-Phase PMSM

Hung-Chi Chen, *Member, IEEE*, Keng-Yuan Chen, and Wei-Yu Chen

***Abstract*—In a six-switch three-phase inverter, the conventional pulsewidth modulation (PWM) has six switching times in every switching period based on the average concept. The used multidimensional feedback quantized modulation (MDFQM) strategy selects one switching state and keeps it in every sampling period based on the minimization of filtered voltage errors between the desired voltage commands and the output voltages. The widths of the output voltage pulse are integer times the fixed sampling time in MDFQM. In this paper, two high-efficiency current control methods based on MDFQM are proposed. They integrate the MDFQM strategy and the current control function to minimize the filtered current errors between the desired current commands and the inverter current. Due to the main advantages of less switching numbers and more closed fundamental current, a high-efficiency performance is achieved. The proposed methods are applied to the current control of a three-phase permanent-magnet synchronous motor. The simulation results and experimental results verify the effectiveness of the proposed methods.**

***Index Terms*—Filtered current error, multidimensional feedback quantized modulation (MDFQM), permanent-magnet synchronous motor (PMSM).**

I. Introduction

In a voltage-source power system, voltage-source inverters (VSIs) are usually used. In order to provide high-quality output voltage, many new pulsewidth-modulation (PWM) methods had been proposed.

From [1] and [2], several conventional PWMs are introduced, such as sine-triangular PWM (SPWM), space vector PWM (SVPWM), and discontinuous PWM (DPWM). The switching numbers of PWM-based methods are proportional to the carrier frequency, and the switching loss is proportional to the switching number. For example, the total switching numbers of SPWM is six times the carrier frequency. Thus, reducing the switching number and decreasing the switching frequency are able to reduce the switching loss and improve the system efficiency.

In [3], the parabolic carrier was introduced to limit the switching frequency and the hysteresis band. The wavelet modulation developed in [4] provides larger fundamental voltage than the conventional SPWM and SVPWM. The finite pulsewidth is considered in SVPWM to reduce the voltage harmonics to reduce the switching number in [5]. The multilevel SVPWM for multiphase VSI with minimum switching number was proposed in [6].

Recently, a new modulation method called multidimensional feedback quantized modulation (MDFQM) has been proposed in [7]. The MDFQM method selects one switching state based on the filtered voltage errors between the voltage commands and the actual output voltages and then keeps the selected switching state until the next sampling time. That is, in MDFQM, the widths of the output voltage pulse are integer times the fixed sampling time. In PWM-based methods, the output voltage pulsewidths are varied from zero to the whole carrier period. The results in [7] clearly show that MDFQM method has less switching number than the carrier-based PWM with a comparable voltage harmonic level.

In addition, PWM methods often integrate the feedback currents to become current control to provide many advantages, such as regulation of the instantaneous current, the peak current protection, and the overload rejection. Current control loops are also able to compensate the effects of the parameter changes, the input voltage change, the voltage drop, and the dead time [8]. Therefore, the current control is an important subject in the modern power electronics, and it has received increasing research interest.

Current control can be divided into two groups. One group is the two-stage control, and the other is one-stage control. The former is the controller cascaded with the PWM method. In [9], each winding current is controlled by a proportional–integral (PI) controller plus the SPWM method. The PI controller is simple, but it is not able to provide closed tracking performance due to the varying current commands. In order to achieve more closed current tracking performance, the feedforward loop [10]–[12], the robust resonant loop in [10] and [12] and the predictive loops with considering the time delay [13], [14], the disturbance [15], and the switching number [16] were proposed. All can be seen as two-stage current control methods.

Hysteresis current control can be seen as one-stage control. The main advantages of the hysteresis current control are

Manuscript received December 4, 2012; revised April 24, 2013, September 29, 2013, and December 18, 2013; accepted February 14, 2014. Date of publication April 9, 2014; date of current version June 6, 2014. This work was supported by the National Science Council (NSC) of Taiwan under Contract NSC 100-2628-E-009-011-MY2.

H.-C. Chen and W.-Y. Chen are with the Department of Electrical and Computer Engineering, National Chiao Tung University, Hsinchu 30010, Taiwan (e-mail: hcchen@cn.nctu.edu.tw).

K.-Y. Chen is with the Department of Electrical Engineering, Yuan Ze University, Chung-Li 32003, Taiwan (e-mail: bettery33@gmail.com).

Color versions of one or more of the figures in this paper are available online at http://ieeexplore.ieee.org.

Digital Object Identifier 10.1109/TIE.2014.2316230

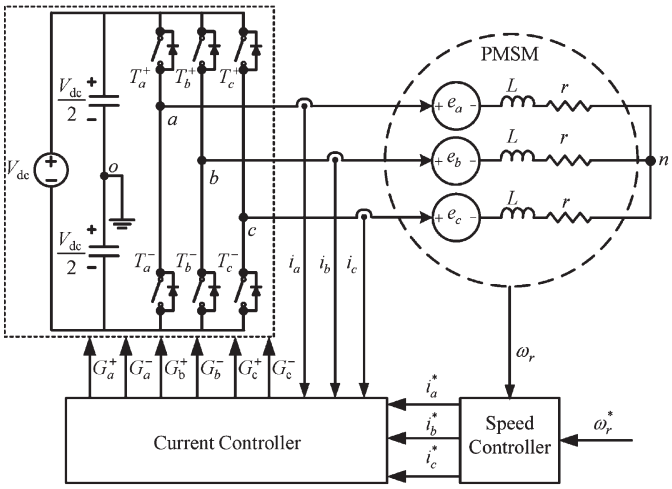

Fig. 1. Three-phase current controller.

simplicity, outstanding robustness, lack of tracking errors, and independence of load parameter changes, but its switching frequency is not fixed. In hysteresis current control, the switching frequency depends largely on the load parameters and varies with the ac voltage. The switching signals are directly obtained by the comparisons of the current references and the current feedbacks with the hysteresis band [17]–[20]. In [17] and [18], there are five hysteresis current control loops to generate the ten switching signals in five phase motors.

The current ripple of the hysteresis current control is limited by the hysteresis band. The smaller the tolerance band is, the larger the switching frequency is. Therefore, the dynamic hysteresis-band control [19], [20] had been proposed to reduce the switching numbers and increase the system efficiency.

In this paper, MDFQM is applied to the current control of three-phase permanent-magnet synchronous motor (PMSM) drives, as shown in Fig. 1, and two MDFQM-based current control methods have been proposed.

The first one is called PI-MDFQM, where each current loop is the simple PI controller cascaded with MDFQM, and it can be seen as a two-stage method. The common PI-SPWM method, i.e., PI current loop cascaded with SPWM [9], is also studied and implemented for comparison. With the same parameters and load conditions, the proposed PI-MDFQM yields higher efficiency and more closed fundamental current than PI-SPWM methods.

The other is named multidimensional feedback quantized current control (MDFQCC), and it can be seen as a one-stage control method. Different from the MDFQM [6] that uses filtered voltage error vector to select the optimal switching state, the proposed MDFQCC method employs the filtered current errors to select the optimal switching state. This selection of the switching state is repeated every sampling time with consideration of the latest current feedbacks and current errors. The most closed fundamental current is provided by the proposed MDFQCC.

The main advantages of the proposed two methods are high power efficiency and closed fundamental current, which are shown in both simulation and experiment results.

II. Two-Stage PI-SPWM Current Control

In this section, conventional PI controller and SPWM are introduced to become PI-SPWM method for comparison. Three current commands i_a^*, i_b^*, and i_c^* are generated by the outer speed controller, and three identified current loops are included to regulate the three inverter currents.

A. Three-Phase Six-Switch VSI

Fig. 1 shows the three-phase VSI and a Y-connected PMSM represented by R-L-e [back electromotive force (EMF)] parameters in series. VSI is composed of six switches T_a^+, T_a^-, T_b^+, T_b^-, T_c^+, and T_c^-. Six switching signals G_a^+, G_a^-, G_b^+, G_b^-, G_c^+, and G_c^- are generated by the current controllers to control the switching devices. In order to avoid short circuit of the input voltage source $V_{\rm dc}$, two gate signals in the same leg are complement, i.e., $G_a^- = \bar{G}_a^+$, $G_b^- = \bar{G}_b^+$, and $G_c^- = \bar{G}_c^+$.

Then, the output voltage corresponding to the midpoint o can be easily represented by the three upper gate signals G_a^+, G_b^+, and G_c^+

$$\begin{bmatrix} v_{ao} \\ v_{bo} \\ v_{co} \end{bmatrix} = V_{\rm dc} \begin{bmatrix} G_a^+ \\ G_b^+ \\ G_c^+ \end{bmatrix} - \frac{V_{\rm dc}}{2} = V_{\rm dc}\mathbf{G}^+ - \frac{V_{\rm dc}}{2}. \quad (1)$$

Then, the voltage v_{no} across the neutral point n and the midpoint o can be expressed by

$$v_{no} = \frac{1}{3}(v_{ao} + v_{bo} + v_{co}) - \frac{1}{3}(v_{an} + v_{bn} + v_{cn}). \quad (2)$$

For a balanced and stable system, three-phase voltages v_{an}, v_{bn}, and v_{cn} are identical with phase shift $2\pi/3$ to each other, and their sum must be zero, i.e., $v_{an} + v_{bn} + v_{cn} = 0$. Therefore, the voltage v_{no} in (2) could be simplified to become $v_{no} - (v_{ao} + v_{bo} + v_{co})/3$, and then, the three-phase voltages can be simplified to

$$\begin{bmatrix} v_{an} \\ v_{bn} \\ v_{cn} \end{bmatrix} = \frac{V_{\rm dc}}{3} \begin{bmatrix} 2 & -1 & -1 \\ -1 & 2 & -1 \\ -1 & -1 & 2 \end{bmatrix} \begin{bmatrix} G_a^+ \\ G_b^+ \\ G_c^+ \end{bmatrix} = \frac{V_{\rm dc}}{3} \begin{bmatrix} 2 & -1 & -1 \\ -1 & 2 & -1 \\ -1 & -1 & 2 \end{bmatrix} \mathbf{G}^+. \quad (3)$$

From (3), the possible combination of three-phase voltages v_{an}, v_{bn}, and v_{cn} can be expressed as

$$\begin{bmatrix} v_{an} \\ v_{bn} \\ v_{cn} \end{bmatrix} \in \left\{ \begin{bmatrix} 0 \\ 0 \\ 0 \end{bmatrix}, \begin{bmatrix} \frac{2V_{\rm dc}}{3} \\ \frac{-V_{\rm dc}}{3} \\ \frac{-V_{\rm dc}}{3} \end{bmatrix}, \begin{bmatrix} \frac{V_{\rm dc}}{3} \\ \frac{V_{\rm dc}}{3} \\ \frac{-2V_{\rm dc}}{3} \end{bmatrix}, \begin{bmatrix} \frac{-V_{\rm dc}}{3} \\ \frac{2V_{\rm dc}}{3} \\ \frac{-V_{\rm dc}}{3} \end{bmatrix}, \begin{bmatrix} \frac{-2V_{\rm dc}}{3} \\ \frac{V_{\rm dc}}{3} \\ \frac{V_{\rm dc}}{3} \end{bmatrix}, \begin{bmatrix} \frac{-V_{\rm dc}}{3} \\ \frac{-V_{\rm dc}}{3} \\ \frac{2V_{\rm dc}}{3} \end{bmatrix}, \begin{bmatrix} \frac{V_{\rm dc}}{3} \\ \frac{-2V_{\rm dc}}{3} \\ \frac{V_{\rm dc}}{3} \end{bmatrix} \right\}. \quad (4)$$

The three upper gate signals G_a^+, G_b^+, and G_c^+ and the resulting phase voltages are tabulated in Table I for reference.

TABLE I
GATE SIGNALS AND THE RESULTING PHASE VOLTAGES

Switching State	G_a^+	G_b^+	G_c^+	v_{an}	v_{bn}	v_{cn}
State 1	0	0	1	$-V_{dc}/3$	$-V_{dc}/3$	$2V_{dc}/3$
State 2	0	1	1	$-2V_{dc}/3$	$V_{dc}/3$	$V_{dc}/3$
State 3	0	1	0	$-V_{dc}/3$	$2V_{dc}/3$	$-V_{dc}/3$
State 4	1	1	0	$V_{dc}/3$	$V_{dc}/3$	$-2V_{dc}/3$
State 5	1	0	0	$2V_{dc}/3$	$-V_{dc}/3$	$-V_{dc}/3$
State 6	1	0	1	$V_{dc}/3$	$-2V_{dc}/3$	$V_{dc}/3$
Zero State	0	0	0	0	0	0
	1	1	1			

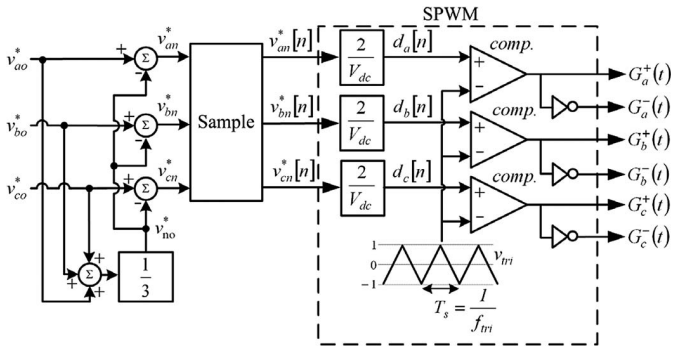

Fig. 2. Block diagram of SPWM.

B. SPWM

The block diagram of SPWM is shown in Fig. 2. Signals v_{ao}^*, v_{bo}^*, and v_{co}^* are the desired voltages. With zero rejection $v_{no}^* = 0$, the desired phase voltages v_{an}^*, v_{bn}^*, and v_{cn}^* are obtained. Through the actions of sampling and normalization, the digital signals d_a, d_b, and d_c are compared with the triangular wave v_{tri} to generate the switching signals for the semiconductor switches.

C. PI Controller

Common PI controllers are used to produce desired phase voltages according to the differences between the desired and the yielded phase current. From Fig. 3, three balanced current commands i_a^*, i_b^*, and i_c^* are generated from the outer speed controller. Then, three command signals v_{ao}^*, v_{bo}^*, and v_{co}^* are calculated by the common PI rule

$$v_{ao}^*[n] = [v_{ao}^*[n-1] + (k_P + k_I)(i_a^*[n] - i_a[n]) - k_P(i_a^*[n-1] - i_a[n-1])] \quad (5)$$

where parameters k_P and k_I are the proportional gain and the integral gain, respectively. It is noted that the limiters of the PI controller output are set to be $\pm V_{\rm dc}/2$ because the maximum SPWM output voltage in the linear modulation region is $V_{\rm dc}/2$.

III. PROPOSED MDFQM-BASED CURRENT CONTROLS

A. MDFQM

Different from SPWM, the carrier-free MDFQM in Fig. 4 considers the filtered voltage error between the desired voltages

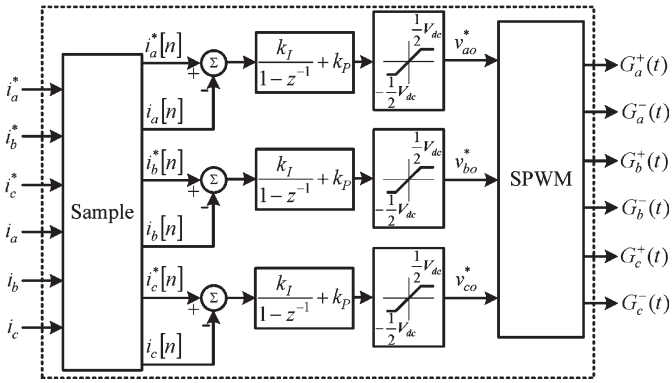

Fig. 3. Block diagram of PI current controller by using SPWM (denoted as PI-SPWM).

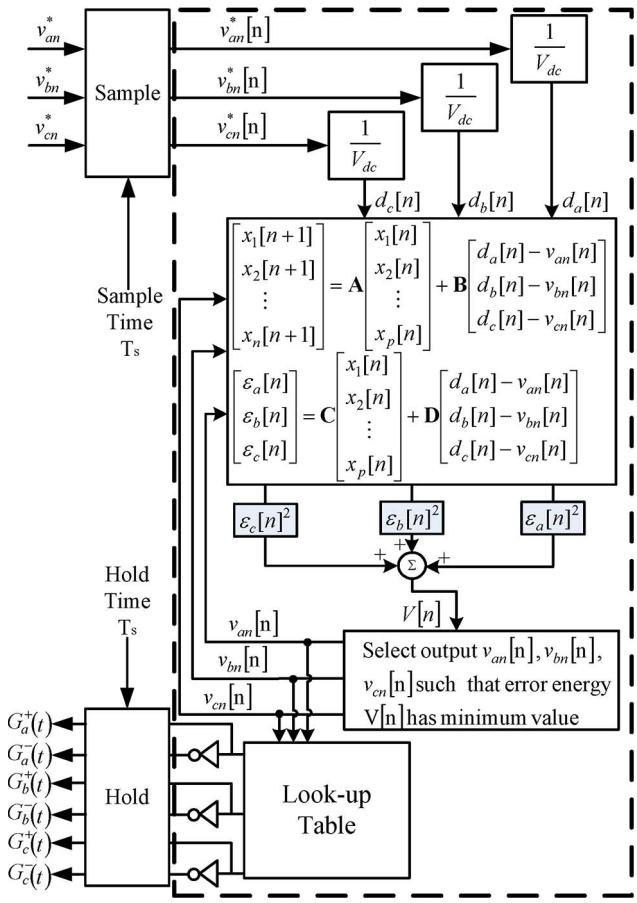

Fig. 4. Block diagram of MDFQM [6].

and the output inverter voltages. As shown in Fig. 4, the desired phase voltages v_{an}^*, v_{bn}^*, and v_{cn}^* are sampled and normalized first. Then, a weighting filter (which is in its state-space form, $\mathbf{A}, \mathbf{B}, \mathbf{C}, \mathbf{D}$) is applied to find the filtered voltage errors ε_a, ε_b, and ε_c. The cost function V is defined as the power of the three filtered voltage errors. Then, the optimal set of v_{an}, v_{bn}, and v_{cn} from the pool (4) is selected based on the minimization of the cost function V. MDFQM algorithm executes every sampling time, and the switching signals keep the latest selection every sampling time T_s. The details of MDFQM can be found in [6].

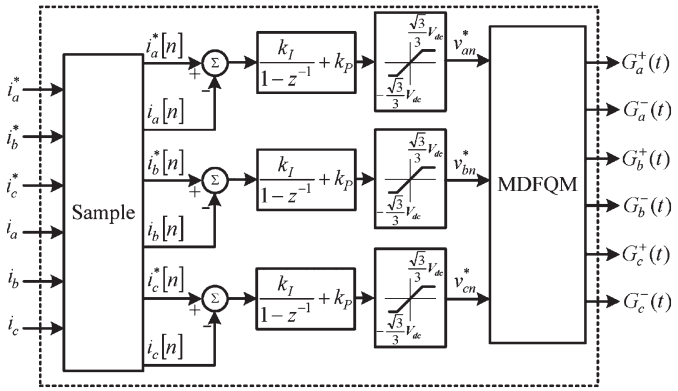

Fig. 5. Block diagram of current controller PI-MDFQM.

The major objective of the VSI is to yield the desired current commands to the load. Two MDFQM-based current controls have been proposed in this section. One is PI-MDFQM, and the other is MDFQCC.

B. PI-MDFQM

The block diagram of the proposed PI-MDFQM has been plotted in Fig. 5. Since the maximum output voltage of MDFQM is $\sqrt{3}V_{\rm dc}/3$ larger than that in SPWM [5], the outputs of PI controllers are limited to $\pm\sqrt{3}V_{\rm dc}/3$.

Furthermore, the pseudofeedback of the phase voltage in MDFQM does not consider the imperfect characteristics of the system such as dead-time effect, rising/falling time, and finite pulsewidth resolution of gating signals. Therefore, the pseudofeedback signals may deviate from the actual phase voltages. These deviations reflect in the current errors and have effect on the generations of the voltage commands by the PI controllers. Then, these deviations reflect in the selection the optimal switching state. That is, there exists a time delay in the two-stage current control methods. However, such time delay can be reduced by the one-stage current control method.

Therefore, the MDFQMCC method is proposed in the next section.

C. MDFQCC

In PI-MDFQM, there are two categories of errors: One is current error input to the current controller, and the other is the voltage error existing in MDFQM. That is, the gate signals are obtained from the current errors and the voltage errors. However, these errors are dependent because the phase voltages and the phase currents can be represented in the same load equations. It means that the original MDFQM is modified to become the proposed MDFQCC including the load parameters. The voltage errors in MDFQM are replaced by the current errors in the proposed MDFQCC.

With referring to the motor model in Fig. 1, we can write (using phase a as an example)

$$i_a(t) = \frac{1}{L}\int_{t}^{t+T} v_{L,a}\,dt \tag{6}$$

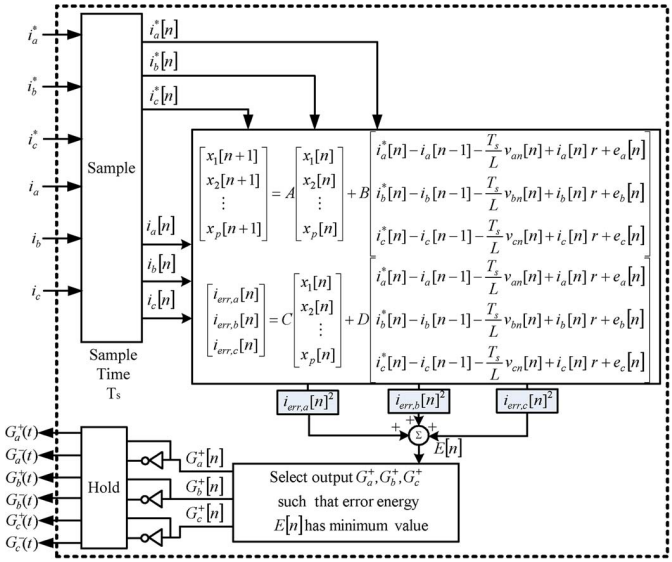

Fig. 6. Block diagram of MDFQCC.

where $v_{L,a}$ is the voltage drop across the inductor of phase a. By considering the discrete time domain, (6) can be approximated as

$$i_a[n] = i_a[n-1] + \frac{1}{L}T_s v_{L,a}[n] \tag{7}$$

where T_s is the sampling period. Furthermore, denote the applied phase voltage as $v_{an}[n]$, and the inductor voltage $v_{L,a}[n]$ can be expressed as

$$v_{L,a}[n] = v_{an}[n] - i_a[n]r - e_a[n]. \tag{8}$$

By combining (7) and (8), the relationships between the sampled phase currents $i_{an}[n]$, $i_{bn}[n]$, and $i_{cn}[n]$ and the sampled phase voltages $v_{an}[n]$, $v_{bn}[n]$, and $v_{cn}[n]$ can be represented as a matrix equation

$$\mathbf{i}[n] = \mathbf{i}[n-1] + \frac{T_s}{L}\left(\mathbf{v}[n] - \mathbf{i}[n]r - \mathbf{e}[n]\right) \tag{9}$$

where $\mathbf{i}[n] = [i_a[n]\ i_b[n]\ i_c[n]]^{\rm T}$, $\mathbf{v}[n] = [v_a[n]\ v_b[n]\ v_c[n]]^{\rm T}$, and the sampled voltage vector $\mathbf{e}[n] = [e_a[n]\ e_b[n]\ e_c[n]]^{\rm T}$ represents the induced back-EMF voltage in the three-phase PMSM.

For the proposed MDFQCC, the cost function E is expressed in terms of the filtered current errors. The filtered current errors can be written in the state-space form (refer to Fig. 6)

$$\begin{aligned}\mathbf{x}[n+1] &= \mathbf{A}\mathbf{x}[n] + \mathbf{B}\left(\mathbf{i}^*[n] - \mathbf{i}[n]\right)\\ \mathbf{i}_{\rm err}[n] &= \mathbf{C}\mathbf{x}[n] + \mathbf{D}\left(\mathbf{i}^*[n] - \mathbf{i}[n]\right)\end{aligned} \tag{10}$$

where $\mathbf{i}^*[n] = [i_a^*[n]\ i_b^*[n]\ i_c^*[n]]^{\rm T}$ is the desired phase current vector and $\mathbf{x}[n]$ denotes the state variables. By substituting (9) into (10), the filtered current errors $\mathbf{i}_{\rm err}[n](=\mathbf{i}^*[n] - \mathbf{i}[n])$ can be rewritten as

$$\begin{aligned}\mathbf{x}[n+1] = \mathbf{A}\mathbf{x}[n] &+ \mathbf{B}\mathbf{i}^*[n] - \mathbf{B}\mathbf{i}[n-1]\\ &- \mathbf{B}\frac{T_s}{L}\left(\mathbf{v}[n] - r\mathbf{i}[n] - \mathbf{e}[n]\right)\end{aligned}$$

$$\mathbf{i}_{\mathrm{err}}[n] = \mathbf{C}\mathbf{x}[n] + \mathbf{D}\mathbf{i}^{*}[n] - \mathbf{D}\mathbf{i}[n-1] - \mathbf{D}\frac{T_s}{L}\left(\mathbf{v}[n] - r\mathbf{i}[n] - \mathbf{e}[n]\right). \quad (11)$$

The cost function $v[n]$ based on the filtered error $\mathbf{i}_{\mathrm{err}}[n]$ is expressed as

$$\begin{aligned} E[n] &= \mathbf{i}_{\mathrm{err}}[n]^{\mathrm{T}}\mathbf{i}_{\mathrm{err}}[n] \\ &= f\left(\mathbf{e}[n], \mathbf{i}^{*}[n], \mathbf{i}[n-1], \mathbf{x}[n]\right) \\ &\quad + \left(\frac{T_s}{L}\mathbf{D}\mathbf{v}[n]\right)^{\mathrm{T}}\left(\frac{T_s}{L}\mathbf{D}\mathbf{v}[n]\right) - 2\left(\frac{T_s}{L}\mathbf{D}\mathbf{v}[n]\right)^{\mathrm{T}} \\ &\quad \times \left(\mathbf{C}\mathbf{x}[n] + \mathbf{D}\mathbf{i}^{*}[n] - \mathbf{D}\mathbf{i}[n-1] \right. \\ &\quad \left. - \frac{T_s}{L}\mathbf{D}\mathbf{i}[n]r - \frac{T_s}{L}\mathbf{D}\mathbf{e}[n]\right) \end{aligned} \quad (12)$$

where the first term $f(\mathbf{e}[n], \mathbf{i}^{*}[n], \mathbf{i}[n-1], \mathbf{x}[n])$ is not a function of the phase voltage vector $\mathbf{v}[n]$, but the other terms are related to the voltage vector $\mathbf{v}[n]$.

To find out the optimal voltage $\mathbf{v}_{\mathrm{opt}}[n]$ to minimize the cost function $E[n]$ in (12), apply the partial differentiation to both sides of (12), and force the resulting equation to zero [5]

$$\frac{\partial\left(\mathbf{i}_{\mathrm{err}}[n]^{\mathrm{T}}\mathbf{i}_{\mathrm{err}}[n]\right)}{\partial\left(\mathbf{D}\mathbf{v}[n]\right)} = 0. \quad (13)$$

The solution to (13) means that the minimum cost function occurs at

$$\mathbf{v}[n] = \frac{L}{T_s}\left(\mathbf{D}^{-1}\mathbf{C}\mathbf{x}[n] + \mathbf{i}^{*}[n] - \mathbf{i}[n-1] - \frac{T_s}{L}\mathbf{i}[n]r - \frac{T_s}{L}\mathbf{e}[n]\right). \quad (14)$$

However, the available $\mathbf{v}_{\mathrm{opt}}[n]$ must be one of the seven voltage vectors in Table I

$$\frac{V_{\mathrm{dc}}}{3}\left\{\begin{bmatrix}0\\0\\0\end{bmatrix}, \begin{bmatrix}1\\1\\-2\end{bmatrix}, \begin{bmatrix}1\\-2\\1\end{bmatrix}, \begin{bmatrix}-2\\1\\1\end{bmatrix}, \begin{bmatrix}-1\\-1\\2\end{bmatrix}, \begin{bmatrix}-1\\2\\-1\end{bmatrix}, \begin{bmatrix}2\\-1\\-1\end{bmatrix}\right\}. \quad (15)$$

Then, the proposed MDFQCC selects the optimal one from the pool (Table I) such that the cost function in (12) has minimum value. The block diagram of the proposed MDFQCC is shown in Fig. 6.

In order to select the optimal voltage $\mathbf{v}_{\mathrm{opt}}[n]$, the normalization and the nearest distance quantization function $q\{.\}$ are used

$$\mathbf{v}_{\mathrm{opt}}[n] = \frac{L}{T_s}\mathbf{D}^{-1}q\left\{\mathbf{C}\mathbf{x}[n] + \mathbf{D}\mathbf{i}^{*}[n] - \mathbf{D}\mathbf{i}[n-1] - \frac{T_s}{L}\mathbf{D}\mathbf{i}[n]r - \frac{T_s}{L}\mathbf{D}\mathbf{e}[n]\right\}. \quad (16)$$

Then, the gate signals are generated according to the following equation from (3):

$$\mathbf{G}^{+}[n] = \mathrm{sign}\left(\mathbf{v}_{\mathrm{opt}}[n]\right) \quad (17)$$

TABLE II
CONTROL PARAMETERS OF THE PLATFORM

DC-link voltage, V_{dc}	$270V$
Calculating frequency, $1/T_s$	$40kHz$
Carrier frequency, f_{tri}	$5kHz$
Dead time	$3\mu s$
PI current controller, k_P	0.00116
PI current controller, k_I	2.619/sec

TABLE III
PMSM PARAMETERS

Stator resistance, $\overline{r}$	1.67Ω per phase
Stator inductance, $\overline{L}$	5.94mH per phase
Mutual inductance, $\overline{M}$	-0.69mH
Back-emf voltage constant (line-to-line), $\overline{K}_v$	37.1 V/krpm
Pole number	4

where the sign function $\mathrm{sign}(x)$ is denoted as

$$\mathrm{sign}(x) = \begin{cases} 1, & \text{when } x \geq 0 \\ 0, & \text{when } x < 0. \end{cases} \quad (18)$$

Both following simulations and experiments are done to confirm the proposed control strategy.

IV. SIMULATION RESULTS

A simulation platform of PMSM motor control is built to verify the proposed current control methods. The block diagram of PMSM control configuration is shown in Fig. 1, where the outer speed control loop generates the three current commands. Two identified PMSMs are coupled together to become an M–G set. The load-side PMSM is connected to the Y-connected resistors R_L. All three current control methods PI-SPWM, PI-MDFQM, and MDFQCC are implemented for comparison. The control parameters and the nominal motor parameters are listed in Tables II and III, respectively.

The weighting matrices of PI-MDFQM and MDFQCC are selected as

$$\mathbf{A} = \begin{bmatrix}1&0&0\\0&1&0\\0&0&1\end{bmatrix} \quad \mathbf{B} = \begin{bmatrix}1&0&0\\0&1&0\\0&0&1\end{bmatrix}$$
$$\mathbf{C} = \begin{bmatrix}1&0&0\\0&1&0\\0&0&1\end{bmatrix} \quad \mathbf{D} = \begin{bmatrix}1&0&0\\0&1&0\\0&0&1\end{bmatrix}. \quad (19)$$

From (19), the filtered voltage errors of MDFQM in Fig. 4 can be simplified to be

$$\varepsilon_k[n] = \varepsilon_k[n-1] + \left(d_k[n] - v_{kn}[n]\right), \qquad k = a, b, c. \quad (20)$$

In Fig. 6, the filtered current errors of MDFQCC are simplified to be

$$i_{\mathrm{err},k}[n] = i_{\mathrm{err},k}[n-1] + i_k^{*}[n] - i_k[n] - \frac{T_s}{L}\left(v_{kn}[n] - e_k[n] - r \cdot i_k[n]\right), \qquad k = a, b, c. \quad (21)$$

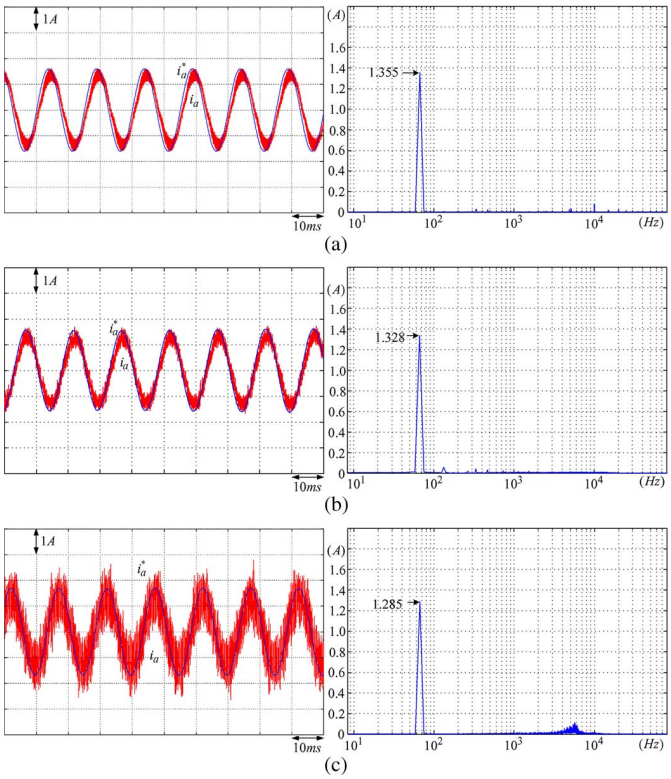

Fig. 7. Simulation of the yielded current and its frequency-domain representation by (a) PI-SPWM, (b) PI-MDFQM, and (c) MDFQCC.

Under the speed command 2000 r/min and the load resistor $R_L = 100\ \Omega$, the inverter currents yielded by PI-SPWM, PI-MDFQM, and MDFQCC are shown in Fig. 7(a)–(c), respectively. The amplitudes of the fundamental current components are also provided by the fast Fourier transform (FFT) method for comparison.

The amplitude of the fundamental current component decreases from 1.355 A in Fig. 7(a) to 1.328 A in Fig. 7(b). It means that, with the same PI parameters, MDFQM is able to provide more closed fundamental current than SPWM.

From Fig. 7(c), the amplitudes of the fundamental current decrease significantly to 1.285 A, which means that the yielded fundamental current of MDFQCC is more closed to the current command than the PI-MDFQM. However, the current ripples of MDFQCC in Fig. 7(c) are larger than that of PI-MDFQM in Fig. 7(b), and thus, the significant current harmonics can be found in the frequency domain in Fig. 7(c).

Under the same load resistance $R_L = 100\ \Omega$ and the same speed command of 2000 r/min (i.e., the same output power), the reduction of the fundamental current amplitude contributes to the reduction of the input power and thus increases the power efficiency.

The total switching numbers of three methods under various speeds are plotted in Fig. 8, where the switching number of PI-SPWM is fixed to 30 K (i.e., six times the carrier frequency).

Moreover, near 20% of the switching number is reduced by the MDFQM-based methods. Furthermore, the switching number of PI-MDFQM is slightly smaller than that of MDFQCC. The smaller the switching number is, the less the switching loss is. It is expected that the proposed methods possess high-efficiency characteristics.

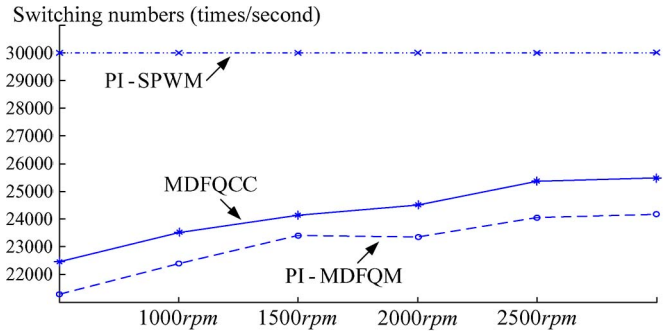

Fig. 8. Switching number of PI-SPWM, PI-MDFQM, and MDFQCC.

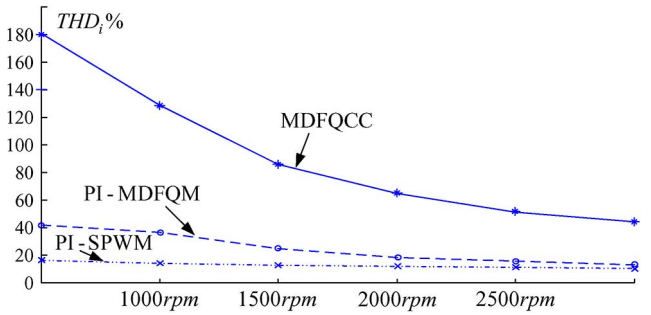

Fig. 9. Current THD values of PI-SPWM, PI-MDFQM, and MDFQCC.

The *total harmonic distortion (THD)* of the current waveforms is defined as

$$\mathrm{THD} = \frac{\sqrt{\sum_{h=2}^{\infty} (i_h)^2}}{i_1} \tag{22}$$

where i_1 is the fundamental current amplitude and i_h $(h \geq 1)$ is the amplitude of the hth-order current harmonic. Fig. 9 shows the calculated THD with various speeds. It is clear that, for THD, PI-SPWM and PI-MDFQM are comparable, particularly at high motor speed. However, MDFQCC yields larger current ripples and introduces larger current harmonics than PI-MDFQM.

Under the sudden change of the amplitude of the current command from 1.5 to 2.5 A at near 2000 r/min, the current waveforms and the switching states with PI-SPWM and PI-MDFQM are plotted in Figs. 10 and 11, respectively. With the same PI parameters, both PI-SPWM and PI-MDFQM methods provide closed current tracking performance. The change of the switching state in the PI-SPWM method is regular without cross-switching, but the change of the switching state in the PI-MDFQM method is not regular.

As shown in Fig. 12, the more closed fundamental current is provided by the proposed MDFQCC method. However, the change of the switching state in MDFQCC is irregular, and cross-switching exists. However, the cross-switching contributes to not only the large current ripple but also the closed fundamental current.

In the two proposed methods, the PI-MDFQM method does not use the motor parameters, and thus, the parameter

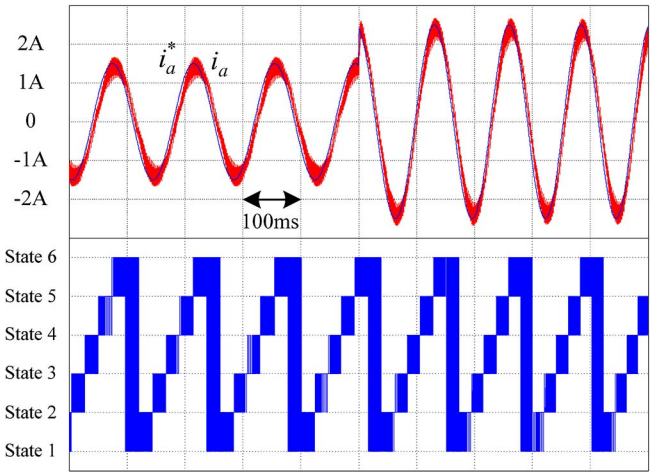

Fig. 10. Transient response and the switching states with the PI-SPWM method.

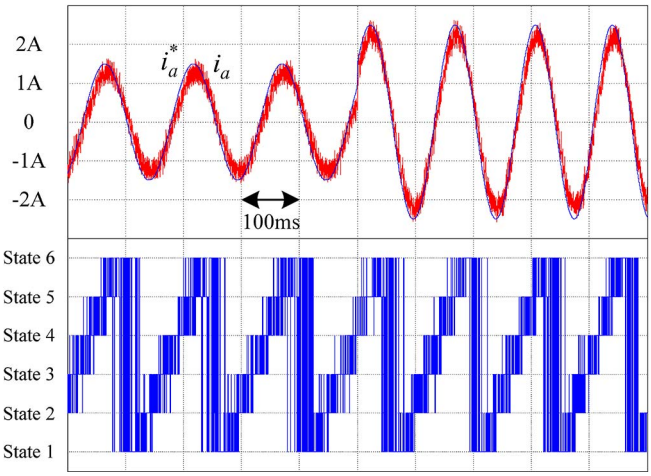

Fig. 11. Transient response and the switching states with the proposed PI-MDFQM method.

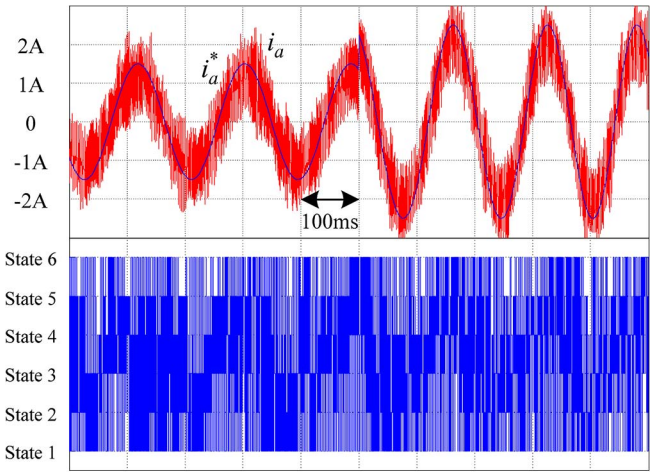

Fig. 12. Transient response and the switching states with the proposed MDFQCC method.

variations would not have an effect on the accuracy of the current regulation and the reported efficiency improvement. However, the MDFQCC method needs the motor parameters.

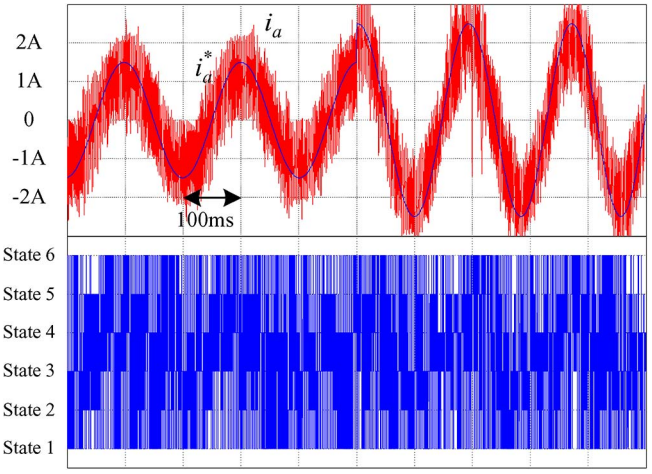

Fig. 13. Transient response with the motor parameter variations for the proposed MDFQCC method.

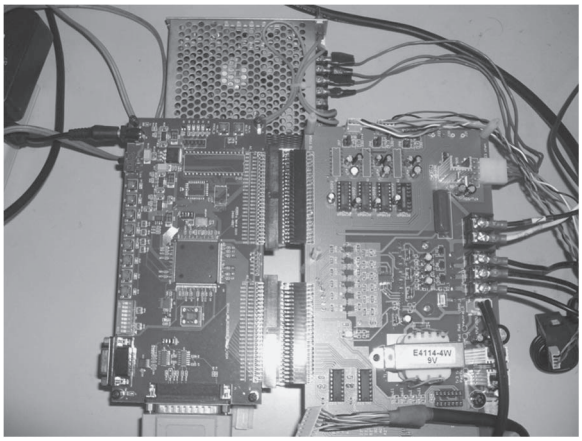

Fig. 14. Picture of the experimental platform.

With the motor parameter variations $r = 12\bar{r}$, $L = 0.8\bar{L}$, $M = 0.8\bar{M}$, and $K_v = 0.8\bar{K}_v$, the current waveforms of the proposed MDFQCC method are plotted in Fig. 13. The parameter variations contribute to the larger current ripples, but the operation is stable and the desired efficiency performance is still achieved.

V. Experimental Results

A. Experimental Platform

To verify and compare the three current controllers, i.e., PI-SPWM, PI-MDFQM, and MDFQCC, a platform based on Xilinx XC3S250E chip (Spartan series) is built (refer to Fig. 14). The configuration of the experimental platform is shown in Fig. 15, where the power module PS21565-P DIP-IPM (Mitsubishi) is used as six-switch VSI. The system and the motor parameters are the same as the simulation parameters listed in Tables II and III.

Due to no A/D and no D/A function in commercial field-programmable gate array (FPGA) XC3S200 chip, external A/D conversion ICs are used to sense the two put currents. Some D/A conversion ICs are used to show the control variables in the scope.

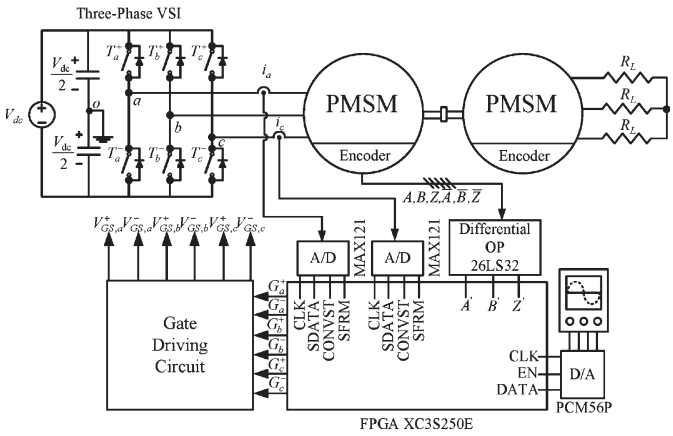

Fig. 15. Configuration of the experimental platform.

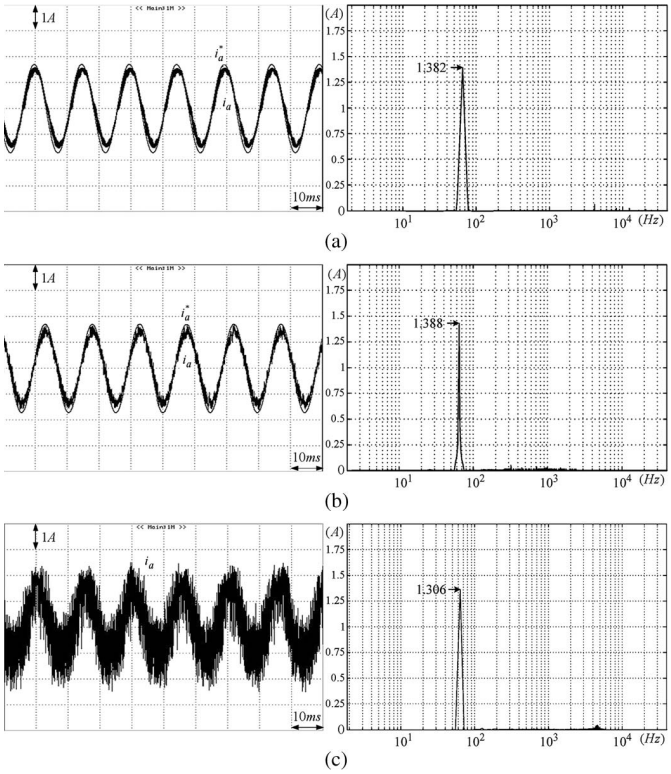

Fig. 16. Experimental current waveforms and their frequency-domain representations by (a) PI-SPWM, (b) PI-MDFQM, and (c) MDFQCC.

B. Current Waveforms

Under the speed command of 2000 r/min and the fixed load resistors $R_L = 100\ \Omega$, the inverter currents i_a yielded by PI-SPWM, PI-MDFQM, and MDFQCC are shown in Fig. 16(a)–(c), respectively. The proposed MDFQM-based methods yield smaller amplitude of the fundamental current component than the PI-SPWM method with the same control parameters. The results agree with the simulation results (refer to Fig. 7).

In Fig. 16, the fundamental current amplitude is reduced from 1.382 A in Fig. 16(a) to 1.306 A in Fig. 16(c) for MDFQCC. It shows that the MDFQCC provides more closed fundamental current component than the other two methods, although the current ripple produced by MDFQCC is larger than those produced by the other methods.

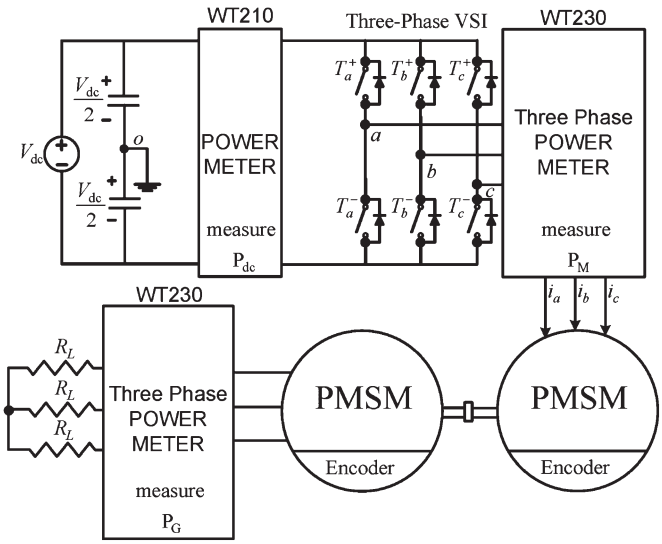

Fig. 17. Block diagram of the power measurement.

C. Efficiency

To address the influence of the switching number, the input power and power efficiency are measured. A single-phase power meter WT210 and two three-phase power meters WT230 are used in the experiment, as shown in Fig. 17. The measured powers $P_{\rm dc}$, P_M, and P_G are the output power of dc-link voltage, output power of three-phase VSI, and dissipated power of the load circuit, respectively.

The efficiency $\eta_{\rm inverter}$ of the three-phase inverter is denoted as P_M divided by $P_{\rm dc}$. Furthermore, the M–G set efficiency η_{MG} and the overall efficiency η are defined as P_G/P_M and $P_G/P_{\rm dc}$, respectively. Because the two identified are coupled together to become an $M-G$ set, the individual motor efficiency can be obtained from the root value of M–G efficiency $\eta_M = \sqrt{\eta_{MG}}$. The efficiency results are plotted in Figs. 18– 20.

From Fig. 18, the inverter efficiency of PI-MDFQM is higher than those of the other methods because the switching number of PI-MDFQM is less than those of the other methods, as shown in Fig. 8. Therefore, reducing the switching number can reduce the switching loss and improve the inverter efficiency effectively.

The M–G efficiency η_{MG} in Fig. 19 shows that the highest η_{MG} is achieved by using MDFQCC due to its closed fundamental current. The more closed fundamental current the method yields, the less input power the system needs.

Thus, for the same speed and load resistors, the efficiency η_{MG} of PI-MDFQM is slightly higher than that of PI-SPWM due to its small switching number. The efficiency η_{MG} of MDFQCC is higher than that of PI-MSFQM with near 5% because MDFQCC provides the more closed fundamental current.

Since the motor efficiency is $\eta_M = \sqrt{\eta_{MG}}$, Fig. 19 also shows that MDFQCC achieves the highest motor efficiency even though the power loss of the current harmonics is considered.

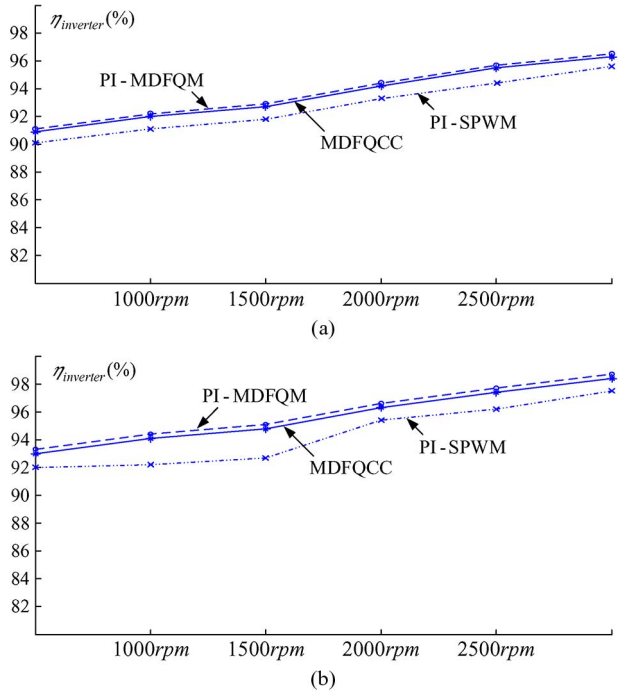

Fig. 18. Inverter efficiency η_{inverter}. (a) $R_L = 100\ \Omega$. (b) $R_L = 50\ \Omega$.

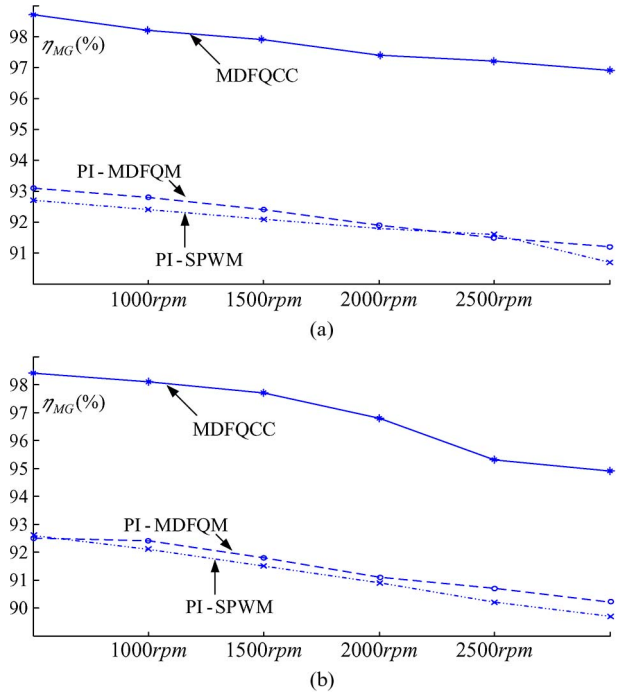

Fig. 19. M–G efficiency η_{MG}. (a) $R_L = 100\ \Omega$. (b) $R_L = 50\ \Omega$.

The overall efficiency η is obtained by multiplying η_{inverter} by M–G efficiency η_{MG}. From Fig. 20, MDFQCC has the higher efficiency than the other two methods. Moreover, the efficiency of PI-MDFQM is higher than that of PI-SPWM.

The current harmonics would result in the additional copper loss and iron loss, but the reduction of the fundamental current would save the copper loss. The measured results show that the proposed MDFQM methods are able to save power loss and provide high-efficiency performance.

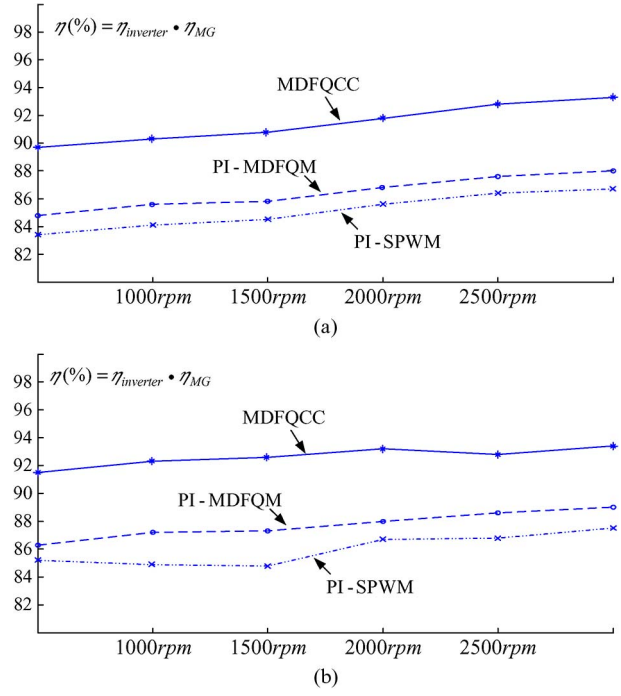

Fig. 20. Overall efficiency η. (a) $R_L = 100\ \Omega$. (b) $R_L = 50\ \Omega$.

The MDFQM proposed in [7] is advanced, and it possesses low switching times and low switching loss. The results show that the proposed MDFQCC is better than both the proposed PI-MDFQM and the conventional PI-SPWM method in the applications of three-phase PMSMs.

From Figs. 4 and 6, both MDFQM-based methods need much more multiply instructions than the conventional SPWM method. From the processor structures of the available microcontroller units (MCUs) and DSPs, the computation burdens of PI-MDFQM and MDFQCC are larger than that of the conventional PI-SPWM method. In the experiment, more than 100 multiply instructions are required to implement MDFQM-based methods. In addition, the available MCUs/DSPs do not provide the MDFQM peripheral, and it is difficult to implement MDFQM in the available MCUs/DSPs.

However, because all parameters of the weighting filters $\mathbf{A}$, $\mathbf{B}$, $\mathbf{C}$, and $\mathbf{D}$ in MDFQM are fixed constants, it is possible to improve the calculation speed of MDFQM by optimizing the processor structure of MCUs/DSPs. In addition, it is not difficult to design the MDFQM peripheral because the authors had implemented MDFQM in FPGA.

Therefore, due to the high-efficiency performance of MDFQM, it is expected to see the appearance of new MCU/DSP supporting MDFQM.

VI. Conclusion

Two MDFQM-based current control methods have been proposed in this paper. One is PI-MDFQM, and the other is MDFQCC. The simulations and experiments are conducted to compare their switching numbers, current harmonics, and power efficiencies.

PI-MDFQM yields less switching number than PI-SPWM, and thus, the former has higher inverter efficiency than the latter

because reducing the switching number can improve inverter efficiency effectively. MDFQCC has more closed fundamental current than PI-MDFQM and PI-SPWM and is able to achieve higher motor efficiency than the other two methods even though the MDFQCC method yields larger current harmonics and current ripples. However, the computation burden of the proposed MDFQM-based current control methods would be the disadvantage, because the available MCUs/DSPs do not support MDFQM peripherals.

The proposed high-efficiency PI-MDFQM and MDFQCC methods can be extended to the other power electronics systems.

REFERENCES

[1] A. M. Hava, R. J. Kerkman, and T. A. Lipo, "Simple analytical and graphical methods for carrier-based PWM-VSI drives," *IEEE Trans. Power Electron.*, vol. 14, no. 1, pp. 49–61, Jan. 1999.

[2] A. M. Hava and E. Un, "Performance analysis of reduced common-mode voltage PWM methods and comparison with standard PWM methods for three-phase voltage-source inverters," *IEEE Trans. Power Electron.*, vol. 24, no. 1, pp. 241–252, Jan. 2009.

[3] G. Wang and Y. W. Li, "Parabolic PWM for current control of voltage-source converters (VSCs)," *IEEE Trans. Ind. Electron.*, vol. 57, no. 10, pp. 3491–3496, Oct. 2010.

[4] S. A. Saleh, C. R. Moloney, and M. Azizur Rahman, "Analysis and development of wavelet modulation for three-phase voltage-source inverters," *IEEE Trans. Ind. Electron.*, vol. 58, no. 8, pp. 3330–3348, Aug. 2011.

[5] K.-Y. Chen and J.-S. Hu, "A filtered SVPWM for multiphase voltage source inverters considering finite pulse-width resolution," *IEEE Trans. Power Electron.*, vol. 27, no. 7, pp. 3107–3118, Jul. 2012.

[6] J.-S. Hu, K.-Y. Chen, T.-Y. Shen, and C.-H. Tang, "Analytical solutions of multilevel space-vector PWM for multiphase voltage source inverters," *IEEE Trans. Power Electron.*, vol. 26, no. 5, pp. 1489–1502, May 2011.

[7] J.-S. Hu, K.-Y. Chen, T.-Y. Shen, and C.-H. Tang, "Control of voltage source inverter using multidimensional feedback quantization modulator," *IEEE Trans. Ind. Electron.*, vol. 58, no. 7, pp. 3027–3036, Jul. 2011.

[8] M. P. Kazmierkowski and L. Malesani, "Current control techniques for three-phase voltage source PWM converters: A survey," *IEEE Trans. Ind. Electron.*, vol. 45, no. 5, pp. 691–703, Oct. 1998.

[9] X. L. Wang, Q. C. Zhong, Z. Q. Deng, and S. Z. Yue, "Current-controlled multiphase slice permanent magnetic bearingless motors with open-circuited phases: Fault-tolerant controllability and its verification," *IEEE Trans. Ind. Electron.*, vol. 59, no. 5, pp. 2059–2062, May 2012.

[10] M.-C. Chou and C.-M. Liaw, "Dynamic control and diagnostic friction estimation for an SPMSM-driven satellite reaction wheel," *IEEE Trans. Ind. Electron.*, vol. 58, no. 10, pp. 4693–4707, Oct. 2011.

[11] G. Dong Olorunfemi, "Current regulation in four-leg voltage-source converters," *IEEE Trans. Ind. Electron.*, vol. 54, no. 4, pp. 2095–2105, Aug. 2007.

[12] M.-C. Chou and C.-M. Liaw, "Development of robust current 2-DOF controllers for a permanent magnet synchronous motor drive with reaction wheel load," *IEEE Trans. Power Electron.*, vol. 24, no. 5, pp. 1304–1320, May 2009.

[13] P. Cortes, J. Rodriguez, C. Silva, and A. Flores, "Delay compensation in model predictive current control of a three-phase inverter," *IEEE Trans. Ind. Electron.*, vol. 59, no. 2, pp. 1323–1325, Feb. 2012.

[14] J. C. Moreno, J. M. Espi Huerta, R. G. Gil, and S. A. Gonzalez, "A robust predictive current control for three-phase grid-connected inverters," *IEEE Trans. Ind. Electron.*, vol. 56, no. 9, pp. 1993–2004, Jun. 2009.

[15] K.-J. Lee, B.-G. Park, R.-Y. Kim, and D.-S. Hyun, "Robust predictive current controller based on a disturbance estimator in a three-phase grid-connected inverter," *IEEE Trans. Power Electron.*, vol. 27, no. 1, pp. 276–283, Jan. 2012.

[16] M. Curkovic, K. Jezernik, and R. Horvat, "FPGA-based predictive sliding mode controller of a three-phase inverter," *IEEE Trans. Ind. Electron.*, vol. 60, no. 2, pp. 637–644, Feb. 2013.

[17] L. Parsa and H. A. Toliyat, "Fault-tolerant interior-permanent-magnet machines for hybrid electric vehicle applications," *IEEE Trans. Veh. Technol.*, vol. 56, no. 4, pp. 1546–1552, Jul. 2007.

[18] S. Sadeghi, L. Guo, H. A. Toliyat, and L. Parsa, "Wide operational speed range of five-phase permanent magnet machines by using different stator winding configurations," *IEEE Trans. Ind. Electron.*, vol. 59, no. 6, pp. 2621–2631, Jun. 2012.

[19] B.-J. Kang and C.-M. Liaw, "A robust hysteresis current-controlled PWM inverter for linear PMSM driven magnetic suspended positioning system," *IEEE Trans. Ind. Electron.*, vol. 48, no. 5, pp. 956–967, Oct. 2001.

[20] N. Prabhakar and M. K. Mishra, "Dynamic hysteresis current control to minimize switching for three-phase four-leg VSI topology to compensate nonlinear load," *IEEE Trans. Power Electron.*, vol. 25, no. 8, pp. 1935–1942, Aug. 2010.

Hung-Chi Chen (M'06) was born in Taichung, Taiwan, in June 1974. He received the B.S. and Ph.D. degrees in electrical engineering from the Department of Electrical Engineering, National Tsing-Hua University, Hsinchu, Taiwan, in 1996 and 2001, respectively.

From October 2001, he was a Researcher with the Energy and Resources Laboratory, Industrial Technology Research Institute, Hsinchu. In August 2006, he joined the Department of Electrical and Control Engineering, National Chiao Tung University, Hsinchu, where he is currently a Professor. From September 2011 to February 2012, he was a Visiting Scholar at the University of Texas, Arlington, TX, USA. His research interests include power electronics, power factor correction, motor and inverter-fed control, and DSP/microcontroller unit/field-programmable-gate-array-based implementation of digital control.

Keng-Yuan Chen received the B.S., M.S., and Ph.D. degrees in electrical control engineering from the Department of Electrical and Control Engineering, National Chiao Tung University, Hsinchu, Taiwan, in 2003, 2005, and 2011, respectively.

From 2011 to 2012, she was a Researcher with the Mechanical and System Laboratory, Industrial Technology Research Institute, Hsinchu. Since 2012, she has been with the Department of Electrical Engineering, Yuan Ze University, Chung-Li, Taiwan. Her research interests include digital signal processing, class-d amplification, and power electronics.

Wei-Yu Chen was born in Taipei, Taiwan, in February 1986. He received the M.S. degree in electrical engineering from the Institute of Electrical Control Engineering, National Chiao Tung University, Hsinchu, Taiwan, in 2011.

His research interests include brushless dc motor control, derivation of new switching methods, design of high-performance power inverter circuits, and FPGA-based implementation of digital control.